Preprints.org

Article

Not peer-reviewed version

Non-Destructive Determination of Surface Residual Stresses in Electron Beam Welded AISI 410 Martensitic Stainless Steel using Magnetic Barkhausen Noise Technique

Hasan İlker Yelbay * and C. Hakan Gür

Posted Date: 28 February 2025

doi: 10.20944/preprints202502.2292.v1

Keywords: Electron Beam Welding; AISI 410 Stainless Steel; Residual Stress; Non-destructive Testing; Finite Element AnalysisMaterial Characterization; Magnetic Barkhausen Noise

Preprints.org is a free multidisciplinary platform providing preprint service that is dedicated to making early versions of research outputs permanently available and citable. Preprints posted at Preprints.org appear in Web of Science, Crossref, Google Scholar, Scilit, Europe PMC.

Copyright: This open access article is published under a Creative Commons CC BY 4.0 license, which permit the free download, distribution, and reuse, provided that the author and preprint are cited in any reuse.

Preprints.org (www.preprints.org) | NOT PEER-REVIEWED | Posted: 28 February 2025 doi:10.20944/preprints202502.2292.v1

Disclaimer/Publisher's Note: The statements, opinions, and data contained in all publications are solely those of the individual author(s) and contributor(s) and not of MDPI and/or the editor(s). MDPI and/or the editor(s) disclaim responsibility for any injury to people or property resulting from any ideas, methods, instructions, or products referred to in the content.

Article

Non-Destructive Determination of Surface Residual Stresses in Electron Beam Welded AISI 410 Martensitic Stainless Steel Using Magnetic Barkhausen Noise Technique

H. İlker Yelbay [1,*] and C. Hakan Gür [2]

[1] Welding Technology and Non-Destructive Testing Center, Middle East Technical University

[2] Metallurgical and Materials Engineering Department, Middle East Technical University

* Correspondence: yelbay@metu.edu.tr

Abstract: Despite their excellent mechanical properties, martensitic stainless steels present significant welding challenges due to their susceptibility to cracking and forming brittle microstructures during thermal cycles. While electron beam welding offers advantages through its high energy density and precise control over conventional welding methods, the induced residual stresses remain a critical concern. This study aims to determine surface residual stresses in electron beam welded AISI 410 martensitic stainless steel using a self-developed C-scan mode Magnetic Barkhausen Noise (MBN) measurement system. A novel calibration and measurement methodology was developed to establish a quantitative relationship between MBN signals and residual stress state. The residual stresses in the welded specimens were analyzed systematically using MBN and X-ray diffraction (XRD) measurements and microstructural characterization. The results revealed a strong correlation between MBN parameters and residual stress states, showing notable variations across the weld zones, i.e., approximately +350 MPa in the heat-affected zone and -50 MPa in the base metal. The experimental findings were also validated through finite element simulations. The correlation between experimental and numerical results confirms the reliability of the proposed MBN-based methodology and system. These findings provide valuable insights for industrial applications, offering a rapid and reliable non-destructive method for residual stress assessment in critical welded components.

Keywords: electron beam welding; AISI 410 stainless steel; residual stress; non-destructive material characterization; magnetic barkhausen noise

1. Introduction

Critical industrial applications requiring safety, high performance, and long service life have forced continual developments in joining and materials characterization technologies. AISI 410 martensitic stainless steel is commonly used in power generation, aerospace, and petrochemical industries. However, its welding has various challenges due to its complex metallurgical behavior and the tendency to form undesirable brittle metastable structures like martensite and residual stresses during thermal cycles [1,2]. Traditional techniques such as tungsten inert gas (TIG) welding and metal inert gas (MIG) welding have been used to join AISI 410 turbine runners and blades, with strict pre- and post-weld controls to diminish the cracking and intergranular corrosion problems. [3,4]. However, their high heat input causes high residual stresses in the material. Electron Beam Welding (EBW) has recently emerged as a promising method with high energy density, a narrow heat-affected zone, and precise control capabilities [5–7]. Compared to conventional methods such as TIG and MIG, EBW employs a significantly reduced heat input, thereby minimizing the residual stresses in components made of AISI 410 steel. However, EBW also creates residual stresses that may

© 2025 by the author(s). Distributed under a Creative Commons CC BY license.

Preprints.org (www.preprints.org) | NOT PEER-REVIEWED | Posted: 28 February 2025 doi:10.20944/preprints202502.2292.v1

negatively affect the mechanical properties and performance leading to early failure of the components [8,12].

The distribution of residual stress in weldments can vary significantly depending on the dominance of shrinkage-induced or transformation-induced mechanisms. Residual stresses cannot be quantified directly; instead, they are calculated by measuring a stress-related parameter. Numerous destructive, semi-destructive, and nondestructive methods exist for measuring stress, some of which can be applied to actual components in the field. Obtaining residual stress maps is ideal for verifying the finite element models. The destructive and semi-destructive methods offer comprehensive information on the distribution of the residual stresses over the whole component, but the component cannot be used after measurement. The most common destructive residual stress measurement techniques include the hole-drilling method (semi-destructive), sectioning method, contour method, slitting (crack compliance) method, and deep-hole drilling method. Nondestructive approaches provide the capacity to monitor the evolution of residual stress in situ or on test specimens. A range of stress measurement methodologies can be employed, with techniques drawing upon the variation of the material's physical characteristics under the action of stresses. Such approaches include measuring elastic strains in specific crystallographic planes via the X-ray diffraction method and measuring the velocity of ultrasonic waves or magnetic parameters. The prevalent problem is the nonlinear relationship between the specific physical characteristic and the residual stress state. Many of them necessitate precise measurements, and in some cases, the results are difficult to interpret. Thus, the successful implementation of nondestructive methods requires the development of sensors for signal capture as well as software for processing and analyzing findings [10].

Standardized methods for measuring residual stress, like X-ray diffraction (XRD) and hole-drilling, are effective but are time-consuming, expensive, or destructive [8,9]. This situation has led to a strong need for reliable, non-destructive methods that can quickly and accurately assess residual stress distributions in welded components. Magnetic Barkhausen Noise (MBN) analysis has become an important non-destructive evaluation method for ferromagnetic materials. This technique detects sudden changes in the movement of magnetic domain walls. The MBN activity of ferromagnetic materials is determined by the interaction of magnetostrictive and elastic lattice strains when cycling the hysteresis curve, and it peaks predominantly in the area around coercivity. To measure MBN, an alternating current is fed into the magnetizing yoke, generating a changing magnetic field based on triangular or sinusoidal functions for repeated magnetization and demagnetization cycles. The progressive breaking of the domain walls causes local magnetic changes, which create pulsed eddy currents in the region of the events. Pulsed eddy currents cause electrical voltage pulses. Capturing these pulses with a pick-up coil produces the Barkhausen noise signal. Because the MBN is derived from magnetization cycles, the sum of rectified bursts simulates the hysteresis loop. MBN measurement offers several advantages, such as high sensitivity to stress states [11–16], fast measurement capabilities [17–19], and the potential for in-situ monitoring [20]. In literature, Barkhausen measurement systems have predominantly been addressed through point-based or line-based measurements. However, in this study, residual stresses across the entire surface of a welded plate were comprehensively mapped using a specially designed MBN measurement system and a detailed 2-D mapping approach. The primary objective of this study is to establish a measurement system that can accurately and reliably determine and map the distribution of the surface residual stresses in martensitic stainless-steel welds.

2. Materials and Methods

2.1. Preparation and Microstructure Characterization of Specimens

The AISI 410 steel plates were extracted from an ingot that was rolled at a temperature of approximately 1200-1250°C. This was followed by annealing within the temperature range of 750-850°C for an extended period, after which the plates were subjected to controlled slow cooling inside

Preprints.org (www.preprints.org) | NOT PEER-REVIEWED | Posted: 28 February 2025 doi:10.20944/preprints202502.2292.v1

the furnace. The plates were cut to dimensions of 160 mm × 160 mm with a thickness of 5.5 mm, then ground and demagnetized before welding. Additionally, the initial MBN values on the plates were measured before the welding process for comparison purposes. For microstructural investigations, the specimens were etched in Vilella's etchant (1 gr. Picric Acid, 5 ml. Hydrochloric Acid in 100 ml. Ethanol) for 7 seconds. This etchant, selectively reveals grain boundaries, martensitic structures, and carbide precipitates through the controlled etching action of hydrochloric acid and picric acid. Optical microscopy (Huvitz HDS-5800) and scanning electron microscopy – energy dispersive spectroscopy (SEM-EDS) investigations were done to characterize the microstructure. The ZEISS Evo MA 15 device was utilized to conduct the measurements, with an accelerated voltage of 20 kV.

2.2. Fixture Design and Welding Process

A special welding fixture (Figure 1) was designed to provide uniform clamping pressure, maintain precise alignment of the plates, allow for thermal expansion during welding, minimize heat sink effects, and ensure reproducible welding conditions. The plates were carefully clamped in the fixture before the welding operation. Each bolt was adjusted to apply a load of 1 kN using a digital torque wrench.

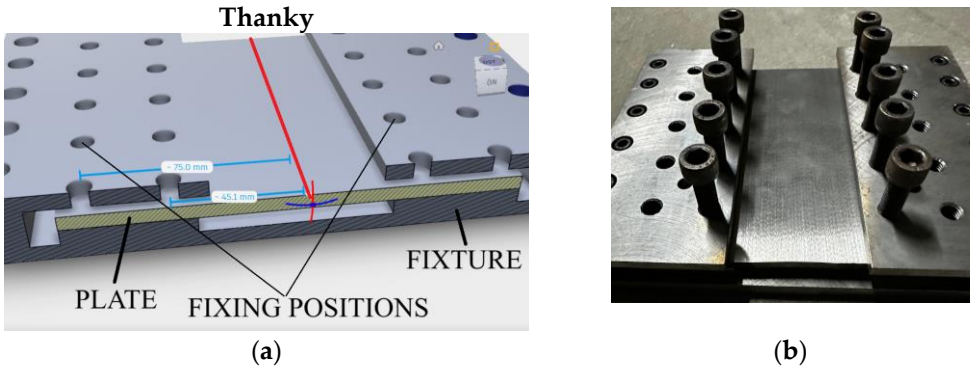

Figure 1. Fixture design (a) and clamping (SF: short fixing, LF: long fixing) positions (b).

The plate was joined in a single pass, creating autogenous butt welds without the addition of filler material using an industrial electron beam welding system under high vacuum (1×10^{-2} Pa) conditions. SST (Steigerwald Strahltechnik) 60 kV 500 mA (30 kW) EBW equipment was used with the parameters listed in Table 1. All parameters were monitored and recorded throughout the process to ensure consistency and repeatability.

Table 1. Electron beam welding parameters.

Voltage (kV)	Current (mA)	Velocity (mm/sec)	Working Distance (mm)	Focus	Pulse	Slope in (mm)	Slope out (mm)
40	42	10	300	Surface - 4 mA	None	10	10

2.3. Magnetic Barkhausen Noise (MBN) Measurements

The MBN measurements were conducted perpendicular to the weld line, encompassing the base material and heat-affected zone (HAZ). The same measurement parameters used in the pre-weld analysis were maintained to ensure consistency. Two different MBN devices, the self-developed device (UNIS-BN) and the commercial Stresstech Microscan RS 500-2 device, were used to compare and validate the measurements. The measurement settings of the devices are given in Table 2.

Table 2. Measurement settings of the MBN devices.

Preprints.org (www.preprints.org) | NOT PEER-REVIEWED | Posted: 28 February 2025 doi:10.20944/preprints202502.2292.v1

Device	Voltage (V)	Frequency (Hz)	Amplification	Magnetization	Filtering (kHz)
Microscan RS 500-2 S1-101-11-01 probe	10	125	10	10	70-200
UNIS-BN	3	100	-	-	10-100

The measurement frequency for the UNIS-BN system was determined by a calibration process (Figure 2). The root mean square (RMS) value was calculated using the Barkhausen signals at the milli-volt (mV) level measured by the probe. Since there is no further significant increase in the RMS value above it, 100 Hz has been selected as the measurement frequency, where the slope of the curve begins to decrease. The analysis depth is approximately 0.1 mm for this magnetization frequency and filtering frequencies (10 – 100 kHz).

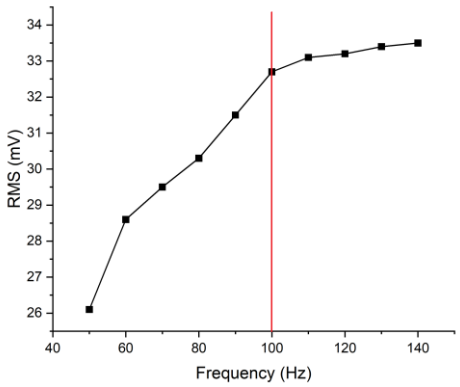

Figure 2. Calibration curve for frequency selection for UNIS-BN device.

The components and working principle of the developed device are illustrated in Figure 3 and Figure 4. Arbitrary waveform generation, voltage regulation, and oscilloscope functionality are utilized with the Digilent Explorer board (EE board), with oscilloscope readings subsequently analyzed via the Waveform software integrated into the same board. The magnetization unit was constructed using a U-shaped core formed from 0.2 mm M3 Grain-Oriented Electrical Steel (GOES) sheets. In the production of transformer magnetic cores, cold-rolled silicon sheet (M3) is employed due to its favorable characteristics, namely low losses and high permeability. The core is wound with 250 turn 36 AWG enameled copper coil windings to generate enough magnetism on the surface. Consequently, the alternating currents passing through the windings generate a longitudinal magnetic field between the two poles of the core. The sensor, comprising a ferrite rod enclosed in a 3 mm diameter vertical 500 turn AWG 44 enameled copper winding to enhance the returning signals. The sensor was situated within a protective zone enveloped in Mu-metal, which shields it from external magnetic fields. This configuration was implemented to prevent the high magnetic fields present in polar regions from influencing the MBN signals. The signals at the millivolt level are received and amplified by a low-noise amplifier and submitted to the software for further processing.

Preprints.org (www.preprints.org) | NOT PEER-REVIEWED | Posted: 28 February 2025 doi:10.20944/preprints202502.2292.v1

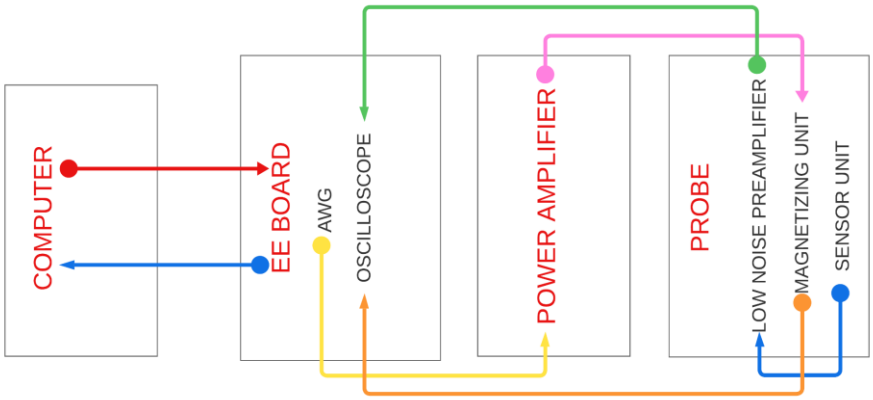

Figure 3. Block diagram of the UNIS-BN device.

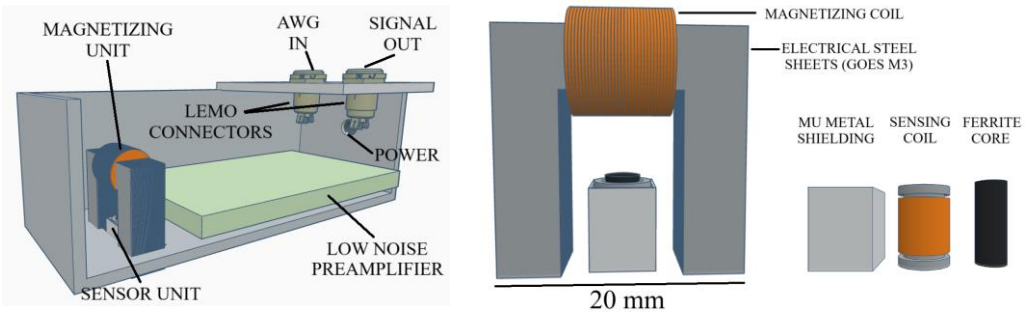

(**a**) (**b**)

Figure 4. Schematic representation of the probe (a), magnetization, and sensor units (b).

The computer-controlled scanner acquired measurements at the specified positions indicated in Figure 5, thereby facilitating the generation of high-resolution surface residual stress maps.

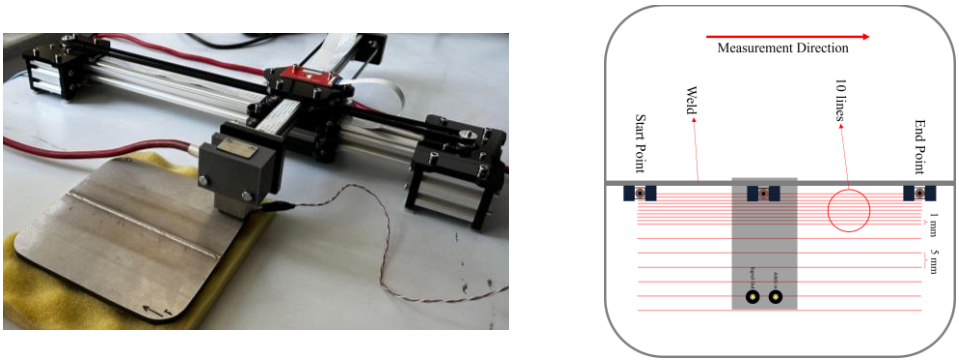

(**a**) (**b**)

Figure 5. Scanner with probe attachment (RS500 Probe) (a) and schematic representation of measurement positions for UNIS-BN probe (b).

The instantaneous signals received from the sensor generate a signal on the software screen against the magnetization curve (Figure 6). In this instance, the mean value of the four MBN signal bursts was recorded as millivolts (mV) for each measurement point.

Preprints.org (www.preprints.org) | NOT PEER-REVIEWED | Posted: 28 February 2025 doi:10.20944/preprints202502.2292.v1

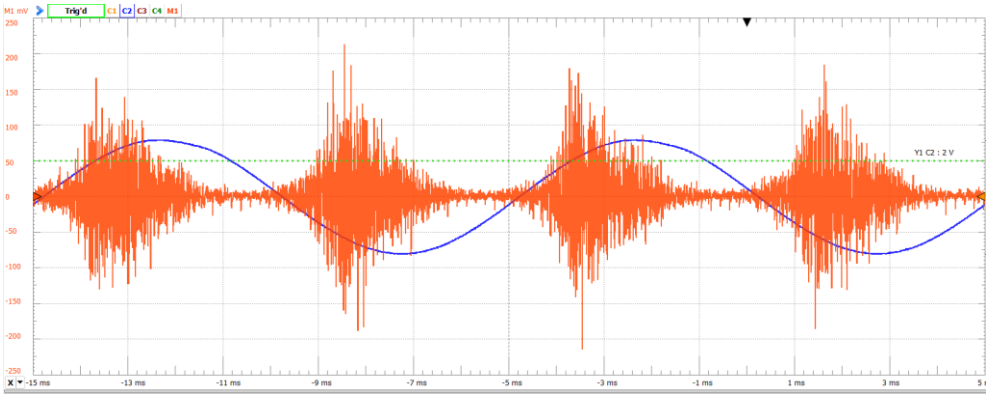

Figure 6. Recorded signals over Waveform software (Blue signal: applied voltage (3V), Orange signal: MBN signals).

A calibration procedure was implemented to establish a quantitative correlation between MBN values and actual stress levels. A rectangular specimen, with dimensions of 150 mm length, 20 mm width, and 5.5 mm thickness, was cut from the welded plate for calibration purposes. A strain gauge (HBM LD20-10/350) was mounted on this specimen to monitor the applied stresses accurately (Figure 7). The specimen was subjected to tensile and compressive elastic loads in a universal testing machine while simultaneously measuring the MBN response. The stress was applied from -87 MPa (compression) to +284 MPa (tension), with measurements taken at regular intervals.

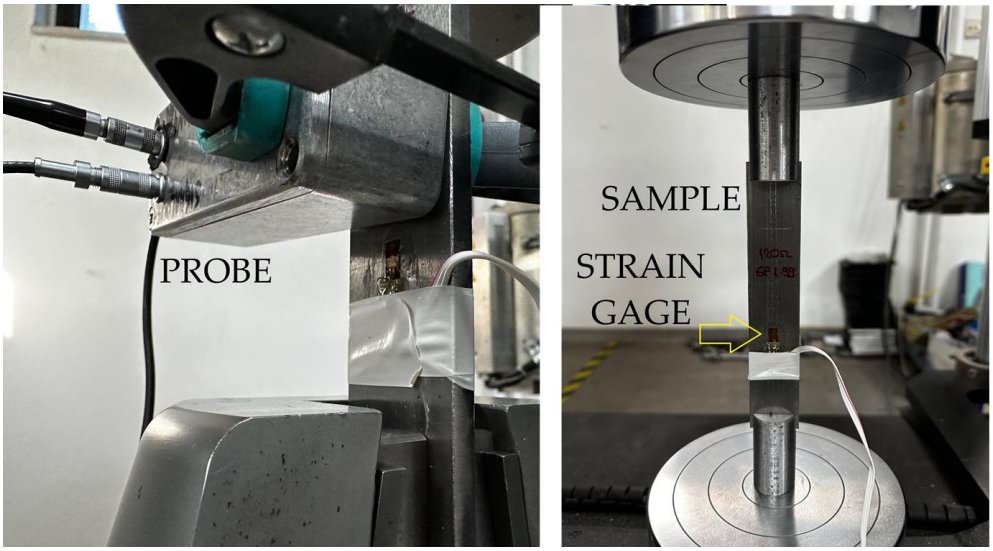

(**a**) (**b**)

Figure 7. Calibration setup (**a**): Probe position (UNIS-BN) (**b**): Strain gauge and sample positioning on the device.

Microhardness measurements were done by applying a load of 1 kg and taking 14 distinct readings in the base metal and weld zone by the Shimadzu HMV-2T system. The measurement depth from the top surface was 0.5 mm, with 1 mm intervals between readings. This approach allowed for detailed mapping of hardness variations and their correlation with the magnetic properties measured through MBN analysis.

For verification of the MBN results, the residual stresses were also measured using the $\sin^2\psi$ XRD method. The XRD technique allows for the measurement of surface residual stresses at depths varying from 5 microns to several tens of microns, influenced by factors such as X-ray wavelength, energy, incidence angle, and the properties of the material. Measurements were taken at a focal length of 2 mm using the Xstress G2R X-ray diffractometer. The Poisson's ratio and Young's modulus values of the AISI 410 plates were calculated as 0.276 and 238 GPa by measuring the transverse and

Preprints.org (www.preprints.org) | NOT PEER-REVIEWED | Posted: 28 February 2025 doi:10.20944/preprints202502.2292.v1

longitudinal sound velocities. The measurements were conducted at 0°, 45° and 90° angles using Cr Kα (λ=2.291Å) X-radiation diffracting from the {211} plane at 156.4° 2θ. Voltage was 30 kV, tube current was 6,7 mA, and measurement time was 10 seconds for each point.

The electron beam/laser welding module within the Simufact Welding software was utilized to perform the thermal analysis and generate the residual stress distribution. The finite element model (FEM) setup and the double-conical volumetric heat source model are illustrated in Figures 8a and 8b. The heat source parameters include an upper radius of 0.5 mm, a lower radius of 0.4 mm, and a penetration depth of 5.5 mm. The finite element mesh consists of 12,516 hexahedral elements and 17,196 nodes, with an element size of 0.625 mm specifically designed for the EBW analysis. To accurately capture the steep thermal gradients, a refined mesh was applied in proximity to the weld zone. A coupled thermomechanical simulation was conducted under boundary conditions involving one bearing and 10 clamping elements. The thermal efficiency for electron beam welding (EBW) was set at 0.95, reflecting minimal heat losses due to the localized heat input and vacuum conditions, whereas the thermal efficiency for tungsten inert gas (TIG) welding was assigned a value of 0.75. The material parameters for elevated temperatures used in the finite element analysis were calculated by JMatPro software and are presented in Figure 9. Additionally, other relevant properties of AISI 410 considered in the analysis are as follows: Poisson's ratio (0.276), liquidus temperature (1510 °C), solidus temperature (1480 °C), and latent heat of fusion (250 kJ/kg).

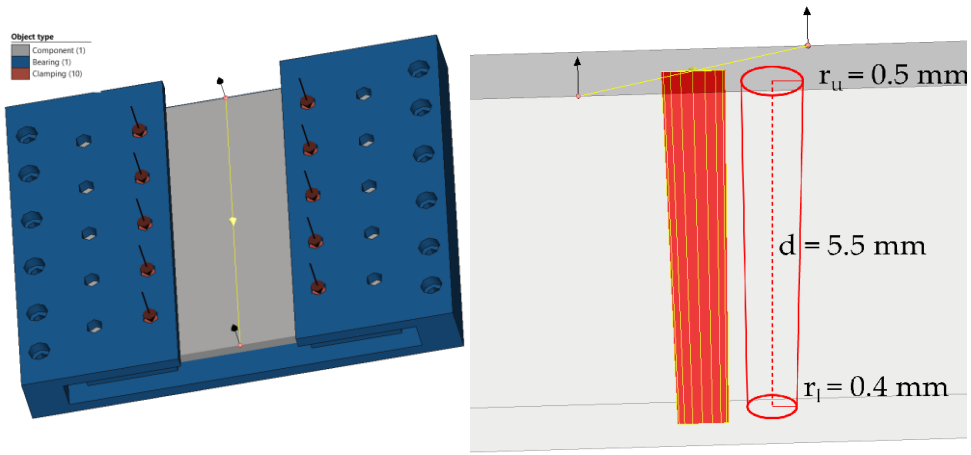

(**a**) (**b**)

Figure 8. FEM analysis setup (component, bearing, and clamping positions) (a) and volumetric heat source model r_u: upper radius, r_l: lower radius (b).

Preprints.org (www.preprints.org) | NOT PEER-REVIEWED | Posted: 28 February 2025 doi:10.20944/preprints202502.2292.v1

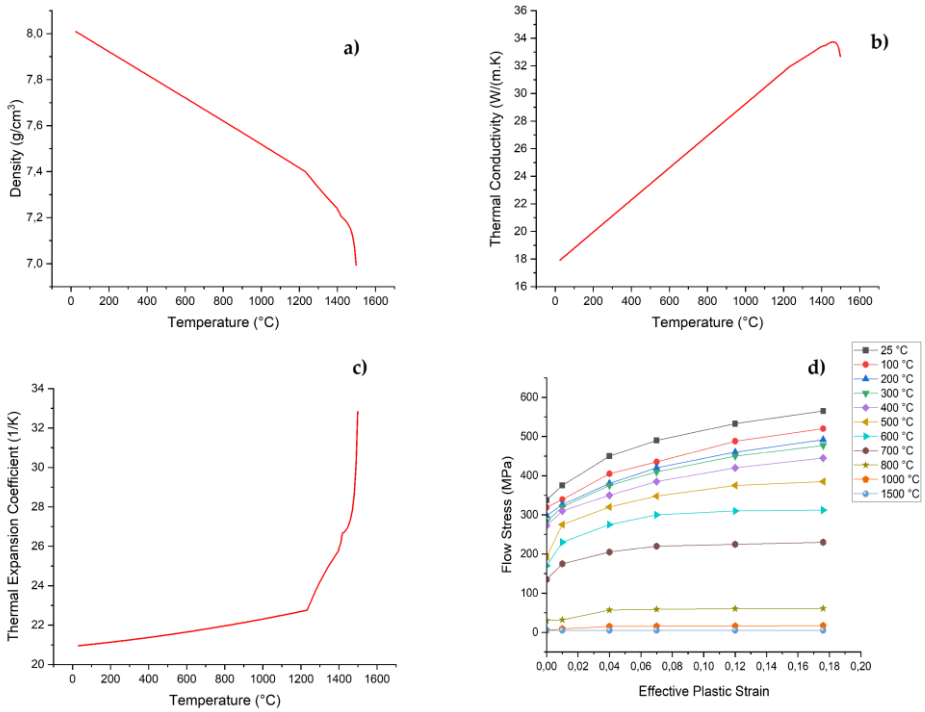

Figure 9. Thermal and mechanical properties of AISI 410 for elevated temperatures calculated by JMatPro software, (a) density, (b) thermal conductivity, (c) thermal expansion coefficient, (d) flow stress curves for strain value of 0.001 1/s.

3. Results and Discussion

The chemical composition of AISI 410 determined via optical emission spectroscopy (Thermo Fisher Scientific iSpark 8860) is given in Table 3. Optical microscopy and SEM-EDS analyses reveal the presence of Cr-rich carbides along the grain boundaries (Figure 10a) and spherical cementite dispersed within the ferrite matrix (Figure 10b). Prolonged exposure at 750–850°C likely facilitates the precipitation of chromium carbides at grain boundaries and cementite formation in the ferrite matrix.

Table 3. Chemical composition of AISI 410 (wt.%).

C	Cr	Mn	Si	P	S	Mo	Ni	V	Al	Cu	Fe
0.14	11.69	0.46	0.45	0.014	0.010	0.03	0.15	0.024	0.010	0.12	Bal.

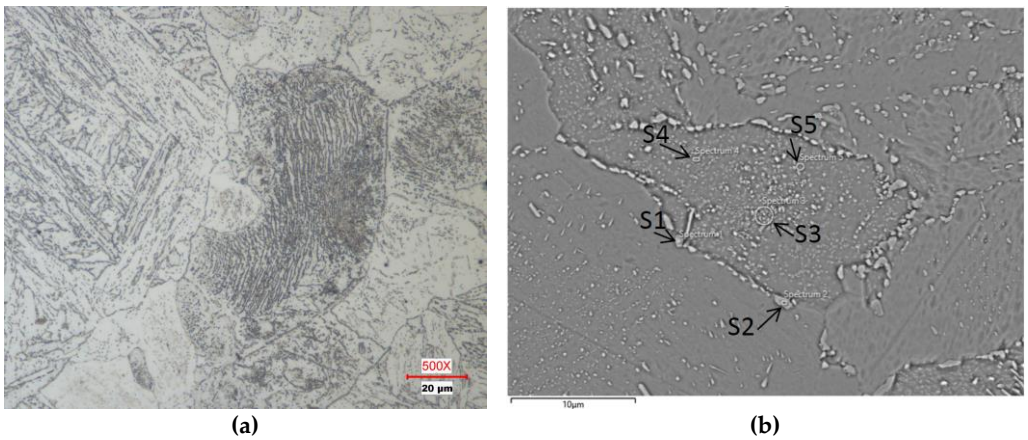

(a) (b)

Figure 10. Representative micrograph of the center region of the base plate (a) and SEM EDS measurement points (b).

Preprints.org (www.preprints.org) | NOT PEER-REVIEWED | Posted: 28 February 2025 doi:10.20944/preprints202502.2292.v1

As shown in Figure 10a, five SEM-EDS measurement points have been identified. Spectra 1 and 2 were acquired from regions suspected to be grain boundary Cr-rich carbide areas, whereas Spectra 3 to 5 represent the ferrite matrix with the spheroidised cementite phase. As presented in Table 4, Spectra 1 and 2 exhibit higher Cr concentrations, confirming the presence of chromium carbides. Similarly, the results of Spectra 3 to 5 indicate a high Fe content, which supports the identification of Fe-rich carbides. Due to the inherent limitations of EDS in accurately quantifying low atomic number elements, the carbon content has been omitted from the reported results to ensure the integrity and reliability of the elemental analysis.

Table 4. Chromium carbide measurement results (At.%).

Spectrum Label	Cr	Fe	Si
S1	60.7	39.3	0
S2	58.9	41.1	0
S3	14.8	84.1	1.1
S4	12.3	86.6	1.1
S5	11.2	87.7	1.1

The heat input in TIG and EBW was compared through FEM analyses (Figure 11). It was confirmed that the three-pass welding required to weld a 5.5 mm-thick part with TIG creates much more heat input to the material. Conversely, EBW could be performed in a single pass, and it was observed that a low amount of residual stresses occurred due to the heat input in a much smaller area.

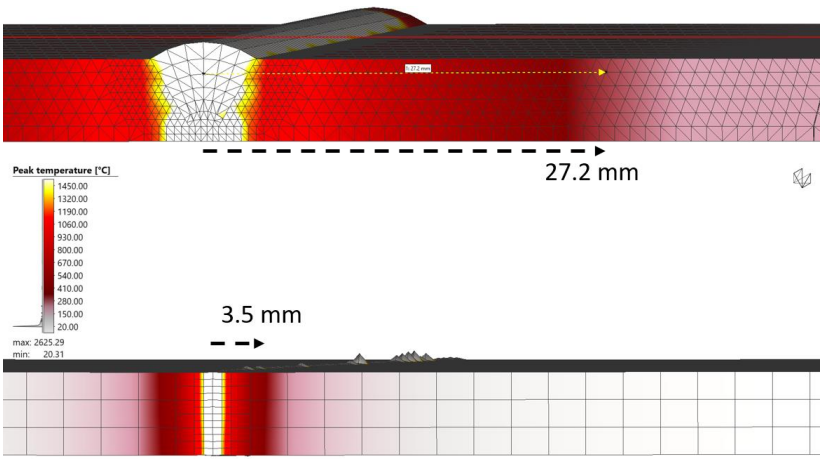

Figure 11. Peak temperature analysis of the TIG welding (above) and EBW (below).

The macro and micro images and hardness profiles of the EBM-SF weld and HAZ are identified and labeled in Figure 12 and Figure 13. The high hardness values (500 HV) and the microstructure in Figure 13 indicate the presence of martensite in the HAZ.

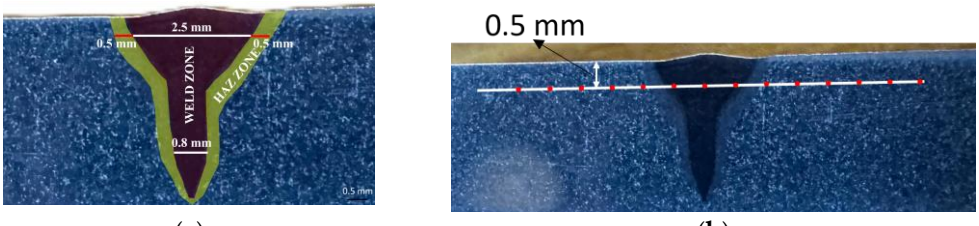

(**a**) (**b**)

Figure 12. EBM-SF sample macro image representing weld and HAZ dimensions (a) and measurement depth and positions (b).

Preprints.org (www.preprints.org) | NOT PEER-REVIEWED | Posted: 28 February 2025 doi:10.20944/preprints202502.2292.v1

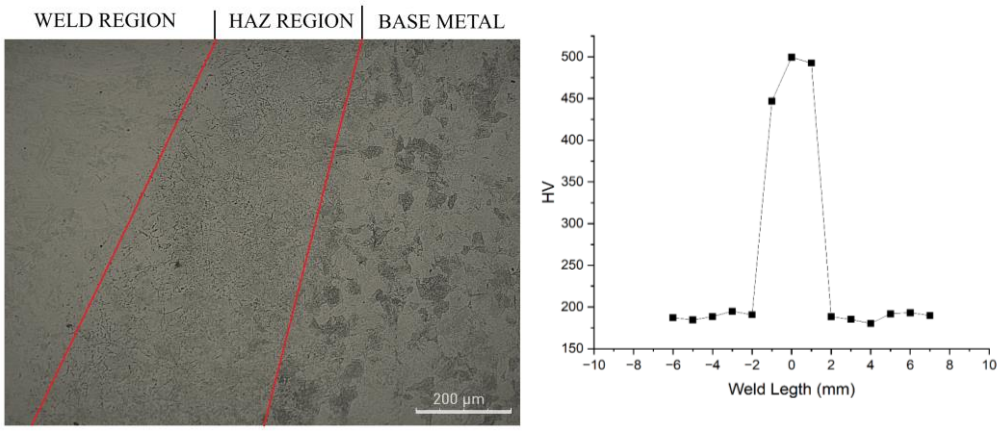

(**a**) (**b**)

Figure 13. EBM-SF micro image representing weld and HAZ (a) and hardness (b) results.

Martensite exhibits a diminishing effect on the MBN signals; therefore, microstructural changes must be considered when constructing calibration curves [10,23]. However, both MBN probes could be positioned 5 mm away from the weld center, and the HAZ width is 2.5 mm from the weld center, the measured values only relate to the microstructure of the base metal. MBN measurements were conducted automatically by connecting the probes to the scanner. The same scanning speed and principle were employed for the measurements in both devices. Since the welded region was not flat, measurement was impossible at a weld width of 3 mm. Furthermore, given that the sensor was situated at a distance of 5 mm from the point where the magnetizing heads were positioned on the welding cap, measurements could be taken at a distance of 5 mm for EBW. As illustrated in Figure 14, the measurement results obtained by two distinct devices on an identical plate demonstrate that the recorded values exhibit a comparable pattern despite the lack of a correlating relationship between the measured values. The difference in the MBN values arises from the distinct physical properties of the two probes. The different size characteristics of the probes, applied voltage, filter range, and pre-amplifier values contribute to the variation in the results. As demonstrated in Figure 15, the results from two distinct probes on the same measurement line (weld length midpoint: 60 mm) are presented as a single graph. A comparison of these results reveals a high degree of consistency, particularly in the left region and the weld area.

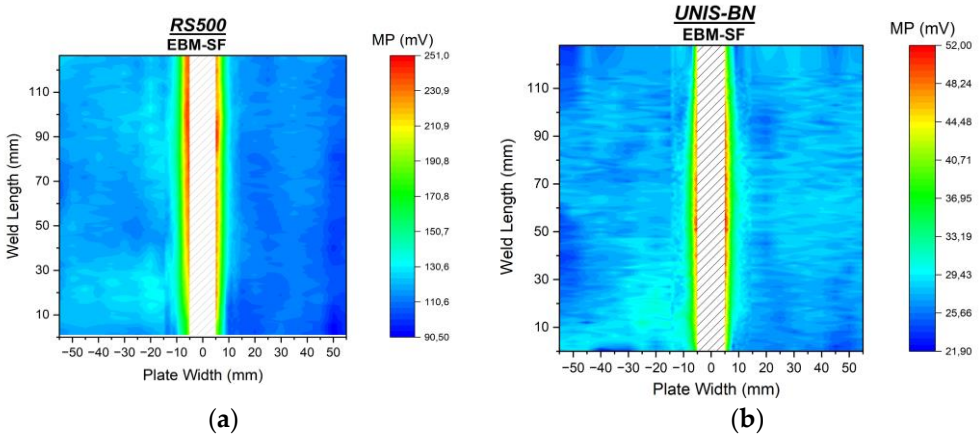

(**a**) (**b**)

Figure 14. MP (magnetic parameter) maps for EBM-SF obtained by RS500 (a) and UNIS-BN (b) devices.

Preprints.org (www.preprints.org) | NOT PEER-REVIEWED | Posted: 28 February 2025 doi:10.20944/preprints202502.2292.v1

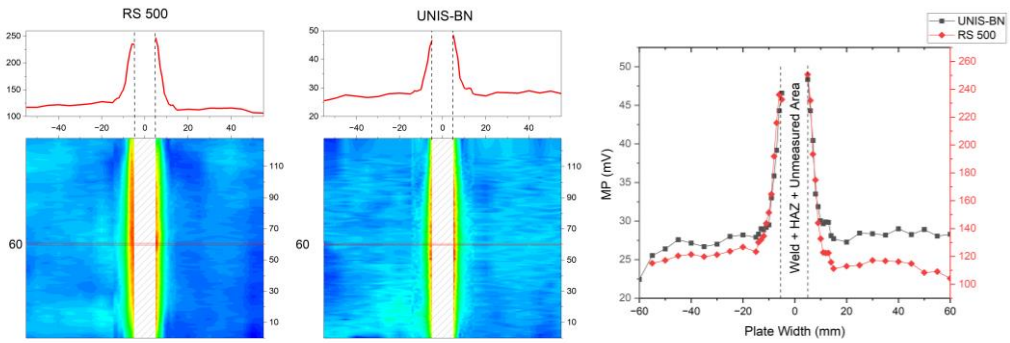

(**a**) (**b**)

Figure 15. Surface map comparison (a) and single line comparison (b) of MP (magnetic parameter) for EBM-SF obtained by RS500 and UNIS-BN devices.

A calibration curve for the base metal (Figure 16) was established to convert the MBN-MP values into residual stresses in MPa. The compressive and tensile load values applied to establish the calibration curve, along with the strain and calculated stress values corresponding to these values, are presented in Table 5. It has been demonstrated that MBN signals increase at tensile stresses and decrease at compressive stresses. The calibration curve obtained in this study is in agreement with the curves in similar studies for base metal calibration [10,22,23]. While the data obtained from the calibration are accurate and usable, a simpler method can be developed for easier application of the calibration procedure with different microstructures under field conditions [24]. Due to the dimensions of the probe contact heads, measurements were restricted to the base metal. Consequently, the calibration curve was constructed exclusively based on the microstructural characteristics of the base metal.

Table 5. The data for establishing the calibration curve.

Load Type	Load (kN)	Strain (μm/m)	MBN (mV)	Stress (MPa)
Compression	10	-365	28,1	-87
	5	-215	28,4	-51
	3	-142	29,1	-34
	1	-65	30	-15
No Load	0	0	31	0
Tension	3	85	33	20
	5	135	33,5	32
	10	275	35,6	65
	20	590	39,1	140
	30	1045	43,1	249
	35	1200	45,1	285

Preprints.org (www.preprints.org) | NOT PEER-REVIEWED | Posted: 28 February 2025 doi:10.20944/preprints202502.2292.v1

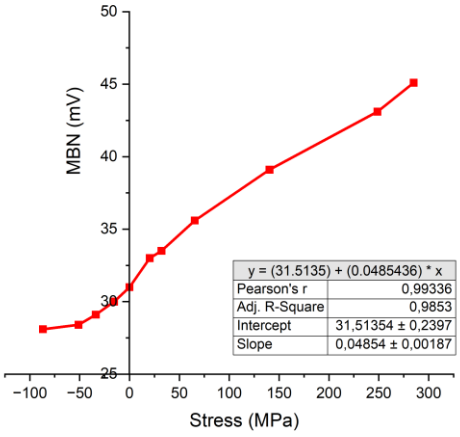

Figure 16. Calibration curve: MBN (mV) versus stress (MPa).

The residual stress data was derived exclusively from the data obtained via the UNIS-BN device, which was recalculated using the calibration curve. The longitudinal stress values exhibited comparable trends to those observed in analogous studies documented in the literature [8,10,22]. The results obtained from the FEM analysis indicate approximately 350-400 MPa tensile residual stress in the vicinity of the HAZ (Figure 17b). The highest tensile residual stresses are typically observed in the region immediately surrounding the weld joint, particularly in the HAZ, due to the effects of thermal cycles and phase transformations during the EBW process. Based on the force equilibrium, the tensile stresses are balanced by the compressive stresses in the base metal.

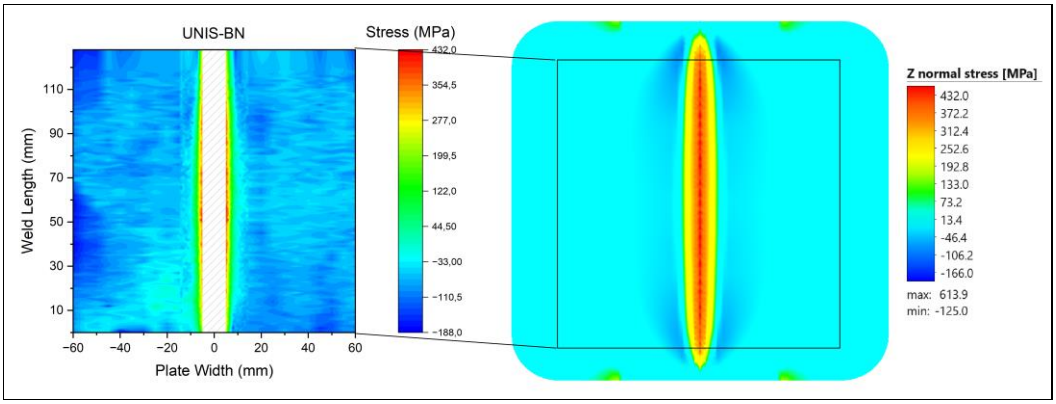

(**a**) (**b**)

Figure 17. The measured longitudinal residual stress data for EBM-SF sample (a) and FEM analysis results (b).

As shown in Figure 18(a), a consistent outcome has been achieved for the residual stress values obtained by MBN, XRD measurements and FEM analysis. The compressive stresses in the base metal determined by the XRD measurements are consistent with the MBN results. Again, the tensile stresses in the HAZ and weld zone give a similar result in the corresponding measurement line (Figure 18b). The XRD measurements did not show equivalent values on both sides of the weldment, probably due to differences in the surface preparation condition of the plate.

Preprints.org (www.preprints.org) | NOT PEER-REVIEWED | Posted: 28 February 2025 doi:10.20944/preprints202502.2292.v1

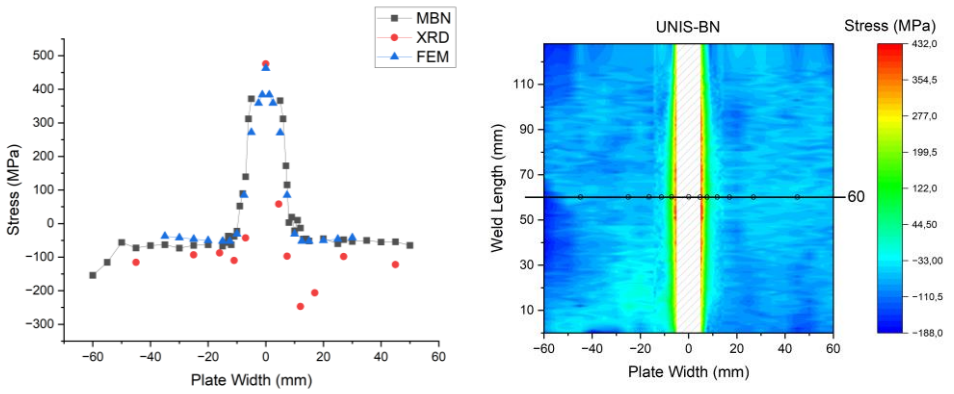

(**a**) (**b**)

Figure 18. Comparison of MBN, XRD and FEM longitudinal residual stress measurement results for the mid-section of the weld.

4. Conclusion

The residual stresses are critical for optimizing the useful lifetime and performance of the components in aerospace, power generation, and manufacturing industries. In this study, a novel Magnetic Barkhausen Noise (MBN) device has been developed and used to determine the surface residual stresses in the AISI 410 plates joined by electron beam welding (EBW). The results were compared and validated with those obtained via a commercial MBN system, XRD measurements, and FE simulations. The following conclusions have been drawn from this particular study:

1. A device and calibration setup has been developed for non-destructive measurement of surface residual stresses. Using the developed MBN system, residual stresses of approximately 350 MPa were measured at a distance of 5 mm in both directions from the weld. These tensile stresses were balanced throughout the base material at around -50 MPa. The results are consistent with the XRD measurements and FE simulations.
2. The proposed C-scan mode of the developed system has proven to be an effective way to obtain fast, reliable, and easily interpretable residual stress maps. It can significantly reduce inspection time and costs in industrial applications.
3. There remain some challenges for further improvement. First, to increase the surface resolution and microstructural analysis, the development of smaller probes and sensors will be beneficial. Second, reference samples should be prepared for different MBN measurement system manufacturers for a standardized calibration procedure. Lastly, the development of a more straightforward and effective calibration system for field applications is a potential avenue for future research.

Author Contributions: Conceptualization, H.İ.Y and C.H.G.; methodology, H.İ.Y and C.H.G.; validation, H.İ.Y; formal analysis, H.İ.Y.; investigation, H.İ.Y; resources, H.İ.Y; data curation, H.İ.Y; writing—original draft preparation, H.İ.Y.; writing—review and editing, H.İ.Y and C.H.G.; visualization, H.İ.Y; supervision, C.H.G. All authors have read and agreed to the published version of the manuscript.

Funding: This research received no external funding.

Institutional Review Board Statement: Not applicable.

Data Availability Statement: Not applicable.

Acknowledgments: The authors would like to thank Mr. Mert Ülker for material supply and tests, Mr. Mert Aygen for the FEM analysis and Mr. Okay Tutar and Mr. Mustafa Işık for the electron beam welding processes.

Preprints.org (www.preprints.org) | NOT PEER-REVIEWED | Posted: 28 February 2025 doi:10.20944/preprints202502.2292.v1

Conflicts of Interest: The authors declare no conflicts of interest.

Abbreviations

The following abbreviations are used in this manuscript:

MBN	Magnetic Barkhausen Noise
AISI	American Iron and Steel Institute
XRD	X-Ray Diffraction
RMS	Root Mean Square
SEM	Scanning Electron Microscopy
EDS	Energy Dispersive Spectrometry
EBW	Electron Beam Welding
AWG	Arbitrary Waveform Generator
AWG	American Wire Gauge
TIG	Tungsten Inert Gas
MIG	Metal Inert Gas

References

1. Lippold J.C, Kotecki D.J. Welding Metallurgy and Weldability of Stainless Steels, Wiley-VCH, March **2005**; pp. 376.
2. Singh R. Welding, Corrosion-Resistant Alloys—Stainless Steel, Applied Welding Engineering Butterworth-Heinemann **2020;** pp. 251-271.
3. Çalık A., Uçar N. Microstructure and Tensile Properties of AISI 410 Stainless Steel Welded TIG Method. IJECS **2023**, *9 (4)*, 394 – 397.
4. Casalino G., Angelastro A., Perulli P., Casavola C., Moramarco V. Study on The Fiber Laser/TIG Weldability of AISI 304 And AISI 410 Dissimilar Weld. J Manuf. Process **2018**, 35, 216-225.
5. Węglowski M.St., Błacha S., Phillips A. Electron beam welding – Techniques and trends – Review, Vacuum **2016**, *130*, 72-92.
6. Tóth T., Hesse A.C., Kárpáti V., Mertinger V., Dilger K. Microstructural and Mechanical Properties of Electron Beam Welded Super Duplex Stainless Steel. *Weld World* **2024,** *68*, 1929–1940.
7. Geľatko M, Vandžura R, Botko F, Hatala M. Electron Beam Welding of Dissimilar Stainless Steel and Maraging Steel Joints. *Materials*. **2024**; 17(23):5769.
8. Feng G., Wang Y., Luo W., Hu L., Deng D. Comparison of Welding Residual Stress and Deformation Induced by Local Vacuum Electron Beam Welding and Metal Active Gas Arc Welding in a Stainless Steel Thick-Plate Joint, *JMT&T* **2021,** *13*, 1967-1979.
9. Li X., Liu J., Wu H., Miao K., Wu H., Li R., Liu C., Fang W., Fan, G. Research Progress of Residual Stress Measurement Methods. *Heliyon* **2024,** *10 (7),* 1-25.
10. Gür, C. H. Review of Residual Stress Measurement by Magnetic Barkhausen Noise Technique, *MPC* **2018,** *7***.** 504-525.
11. Sarafan S., Wanjara P., Gholipour J., Champliaud H. Global and Local Characteristics of an Autogenous Single Pass Electron Beam Weld in Thick Gage UNS S41500 Steel, *Materials Science and Engineering: A* **2016**, *666*, 360-371.
12. Yelbay, H. I., Gür C. H., Çam I. Non-Destructive Determination of Residual Stress State in Steel Weldments by Magnetic Barkhausen Noise Technique. *NDT & E International* **2010**, *43(1)*, 29-33.
13. Gurruchaga, K., Lasaosa, A., Artetxe, I., Martínez-de-Guerenu, A. Grinding Burn Detection via Magnetic Barkhausen Noise Analysis Independently of Induction Hardened Depth. *Materials* **2023**, *16*, 2127.
14. Wang, X., Cai, Y., Liu, X., He, C. Quantitative Prediction of Surface Hardness in Cr12MoV Steel and S136 Steel with Two Magnetic Barkhausen Noise Feature Extraction Methods. *Sensors* **2024**, *24*, 2051.
15. Neslušan, M., Bahleda, F., Minárik, P., Zgútová, K. & Jambor, M. Non-Destructive Monitoring of Corrosion Extent in Steel Rope Wires Via Barkhausen Noise Emission. *JMMM* **2019**, *484*, 179-187.
16. Neslušan, M., Minárik, P., Čep, R., Ondruš, J., Pitoňák, M., Zgútová, K. Measurement of Bearing Capacity of Steel Road Barrier Flange Via Barkhausen Noise Emission, *Engineering Failure Analysis* **2024**, *156*, 107804.

Preprints.org (www.preprints.org) | NOT PEER-REVIEWED | Posted: 28 February 2025 doi:10.20944/preprints202502.2292.v1

17. Hristoforou EV. Permeability Sensors for Magnetic Steel Structural Health Monitoring. *Sensors*. **2025**; *25(3)*, 606.
18. Staub A, Scherer M, Zehnder P, Spierings AB, Wegener K. Residual Stresses Measurements in Laser Powder Bed Fusion Using Barkhausen Noise Analysis. *Materials* **2022**; *15(7)*, 2676.
19. Barkhausen Noise Inspection for Detecting Grinding Burns in High Strength Steel Parts, SAE International, Aerospace Recommended Practice, ARP4462
20. Rößler M., Putz M., Hochmuthv C., Gentzen J. In-Process Evaluation of The Grinding Process Using a New Barkhausen Noise Method, P*rocedia CIRP* **2021,** *99*, 202-207.
21. Avila, J. A., Conde, F. F., Pinto, H. C., Rodriguez, J., & Grijalba, F. A. F. Microstructural and Residuals Stress Analysis of Friction Stir Welding of X80 Pipeline Steel Plates Using Magnetic Barkhausen Noise. *Journal of Nondestructive Evaluation* **2019**; *38*(4), 86. https://doi.org/10.1007/s10921-019-0625-2
22. Liskevych, O., Fiorin, A. P. F., Almeida, E. M. de, Feijó, G. F., Oliveira, R. L. M. de, & Macêdo, M. C. S. de. An Experimental Approach for Correlation of the Magnetic Barkhausen Noise to Microstructural Changes and Residual Stress in Welding Joints. *Soldagem & Inspeção* **2024**, *29*. https://doi.org/10.1590/0104-9224/si29.08
23. Vourna, P., Ktena, A., Tsakiridis, P. E., & Hristoforou, E. A Novel Approach of Accurately Evaluating Residual Stress and Microstructure of Welded Electrical Steels. *NDT & E International* **2015**, *71*, 33–42. https://doi.org/10.1016/j.ndteint.2014.09.011
24. Garstka, T.; Szota, P.; Mróz, S.; Stradomski, G.; Gróbarczyk, J.; Gryczkowski, R. Calibration Method of Measuring Heads for Testing Residual Stresses in Sheet Metal Using the Barkhausen Method. *Materials* **2024**, *17*, 4584. https://doi.org/10.3390/ma17184584

Disclaimer/Publisher's Note: The statements, opinions and data contained in all publications are solely those of the individual author(s) and contributor(s) and not of MDPI and/or the editor(s). MDPI and/or the editor(s) disclaim responsibility for any injury to people or property resulting from any ideas, methods, instructions or products referred to in the content.